Disappearance, recovery and patchiness of plasmaspheric hiss following two consecutive interplanetary shocks: First results

S. Chakraborty[1], D. Chakrabarty[1], G. D. Reeves[2], D. N. Baker[3], S. G. Claudepierre[4,5], A. W. Breneman[6], D. P. Hartley[7], B. A. Larsen[2]

[1]Physical Research Laboratory, Ahmedabad, Gujrat, India
[2]Space Science and Applications Group, Los Alamos National Laboratory, Los Alamos, New Mexico, USA
[3]Laboratory for Atmospheric and Space Physics, University of Colorado Boulder, Boulder, Colorado, USA
[4]Space Sciences Department, The Aerospace Corporation, El Segundo, California, USA
[5]Department of Atmospheric and Oceanic Sciences, University of California, Los Angeles, CA, USA
[6]School of Physics and Astronomy, University of Minnesota, Twin Cities, Minneapolis, MN, USA
[7]Department of Physics and Astronomy, University of Iowa, Iowa City, IA, USA

Key Points:

- First report on plasmaspheric hiss variability in response to two successive interplanetary shocks observed by the Van Allen probes.
- Both the shocks triggered substorms that played important roles in the variability of plasmapsheric hiss.
- Based on detailed electron phase space density and wave growth rate analyses, the observed hiss variations are explained.

Corresponding author: Suman Chakraborty, `suman.chakrabarty37@gmail.com`

Abstract

We present, for the first time, a plasmaspheric hiss event observed by the Van Allen probes in response to two successive interplanetary shocks occurring within an interval of ∼2 hours on December 19, 2015. The first shock arrived at 16:16 UT and caused disappearance of hiss for ∼30 minutes. Significant Landau damping by suprathermal electrons followed by their gradual removal by magnetospheric compression opposed the generation of hiss causing the disappearance. Calculation of electron phase space density and linear wave growth rates showed that the shock did not change the growth rate of whistler mode waves within the core frequency range of plasmaspheric hiss (0.1 - 0.5 kHz) during this interval making conditions unfavorable for the generation of the waves. The recovery began at ∼16:45 UT which is attributed to an enhancement in local plasma instability initiated by the first shock-induced substorm and additional possible contribution from chorus waves. This time, the wave growth rate peaked within the core frequency range (∼350 Hz). The second shock arrived at 18:02 UT and generated patchy hiss persisting up to ∼19:00 UT. It is shown that an enhanced growth rate and additional contribution from shock-induced poloidal Pc5 mode (periodicity ∼240 sec) ULF waves resulted in the excitation of hiss waves during this period. The hiss wave amplitudes were found to be additionally modulated by background plasma density and fluctuating plasmapause location. The investigation highlights the important roles of interplanetary shocks, substorms, ULF waves and background plasma density in the variability of plasmaspheric hiss.

Plain Language Summary

Plasmaspheric hiss waves are whistler-mode, low frequency electromagnetic emissions found inside the dense plasmasphere and duskside plasmaspheric plumes. These waves play important role in controlling radiation belt dynamics by efficiently scattering electrons leading to their precipitation into the atmosphere. Therefore, understanding their variability is an important topic in radiation belt studies. Earlier studies on plasmaspheric hiss waves showed their intensification as well as disappearance following a single interplanetary shock impact. In this study, we provide the first direct observational evidence of plasmaspheric hiss variability in response to two consecutive interplanetary shocks hitting the magnetosphere within an interval of ∼2 hours based on unique observations by the twin Van Allen probes. Based on these observations and supported by detailed linear wave growth rate and phase space density analyses, it is shown that substorms triggered by both the interplanetary shocks and ULF waves generated after the second shock modulated the plasmaspheric hiss wave intensities in a significant manner. The amplitudes of the hiss waves are also found to be modulated by background plasma density and fluctuating plasmapause location.

1 Introduction

Plasmaspheric hiss waves are mostly structureless, low frequency (100 Hz to few kHz) broadband whistler mode electromagnetic emissions confined inside the high-density plasmasphere and duskside plasmaspheric plumes (Dunckel & Helliwell, 1969; Russell et al., 1969; Meredith et al., 2004; Summers et al., 2008). These waves are widely distributed in radial distance and magnetic local time (MLT), although the strongest emissions are observed typically near the dayside plasmasphere, around the local noon (12 MLT) (Li et al., 2015; Spasojevic et al., 2015). They are detected during both geomagnetic quiet and disturbed periods, with wave amplitudes varying from a few tens of picotesla during quiet times and enhancing up to ∼100 pT during enhanced geomagnetic activity. Their origin and spatial distribution are an attractive subject of radiation belt studies as these waves are known to play an important role in controlling radiation belt dynamics by causing pitch angle scattering and subsequent atmospheric precipitation

of electrons (from tens of keV to few MeV) via cyclotron resonance in a time span of several days to weeks (e.g., Thorne et al. (2013); Li et al. (2015); Ripoll et al. (2017)).

Since the discovery of hiss waves in the magnetosphere by Russell et al. (1969), numerous studies have been done concerning the wave properties. Thorne et al. (1979) proposed the generation of plasmaspheric hiss waves during geomagnetic quiet times as due to amplification of trapped waves near an equatorial region just inside the plasmapause. During geomagnetic active periods, both local amplification of hiss inside the plasmasphere by electron cyclotron instability and external sources like chorus waves are proposed to contribute. Chum and Santolik (2005), using ray tracing theoretical simulation, investigated the ray trajectories of nonductedly propagating lower band whistler mode chorus waves with respect to their initial angle θ_0 (the angle between the wave vector and the ambient magnetic field). It was found that if the initial wave vector is deviated from the ambient magnetic field towards lower L-shells (directed to the Earth) by an angle greater than θ_B, which was termed the bifurcation angle, the wave may, after reflection, propagate into the plasmasphere and evolve into plasmaspheric hiss. Santolik et al. (2006) found discrete time-frequency structures in low altitude ELF hiss recorded by Freja and DEMETER spacecraft at altitudes of 700 – 1200 km that resembled with the time-frequency structure and frequencies of chorus recorded by Cluster spacecraft at radial distances of 4 – 5 Earth radii. They used backward ray tracing techniques to follow the hiss waves to their anticipated source region. This was consistent with the theoretical results of Chum and Santolik (2005) and both the studies showed that earthward propagating chorus waves could be considered as possible candidates for plasmaspheric hiss. Later, by ray tracing technique and supported by observations, Bortnik et al. (2008, 2009, 2011) and Chen et al. (2012a) suggested that hiss waves can originate by propagation of chorus waves from an equatorial source region outside the plasmasphere to higher latitudes and subsequent refraction into the plasmasphere which then evolves into plasmaspheric hiss. Agapitov et al. (2018) used 11 years of multipoint wave measurement data during the interval 2007 – 2017 from five Time History of Events and Macroscale Interactions during Substorms (THEMIS) spacecraft covering $L = 2$ to 10 at low magnetic latitudes and over all magnetic local times (MLTs) to study the spatial extent and wave power distributions of both chorus and hiss waves in the proximity of their respective generation regions and also to statistically examine any possible link between these two waves. From the statistical results, significant temporal correlations were found between chorus (outside the plasmasphere) and hiss (inside the plasmasphere). They found that 20% of chorus waves observed during the 11-year interval of study were well correlated with hiss waves usually detected with a delay less than 10 seconds with a correlation > 0.7 between their wave power dynamics. Such well correlated chorus and hiss waves were also found to be separated by $\sim$2 – 3 Earth radii in the radial direction, the hiss waves typically observed 1 – 2 hrs later in MLT than the chorus waves. But recently, using observations from Van Allen Probes and coupled with ray tracing simulations, Hartley et al. (2019) showed that the chorus-to-hiss mechanism exists for only a small spatial region close to the outer edge of the duskside plasmaspheric plume where strong azimuthal density gradients are present. This study is in contrast to the previous understanding and implies that it is unlikely for chorus emissions to contribute significantly to the plasmaspheric hiss wave power.

Plasmaspheric hiss wave power has been found to vary significantly with geomagnetic activities (Meredith et al., 2004; Green et al., 2005; Agapitov et al., 2013; Spasojevic et al., 2015; Orlova et al., 2016; Mourenas et al., 2017; Claudepierre et al., 2020). Tsurutani et al. (2015), using one year interval of Polar data studied the dependence of plasmaspheric hiss on geomagnetic activity, especially AE and $SYM-H$ indices. From their study, they found that the hiss waves can be found during intervals of both high AE and low AE, majority of the waves being detected with $AE < 250$ nT or during geomagnetic quiet times. One interesting finding from this study was that plasmaspheric hiss waves were found to intensify during intervals of high positive $SYM - H$ values

which correspond to high solar wind ram pressure events. They concluded that when enhanced solar wind compresses the magnetosphere, the wave intensities become larger probably due to energetic electrons drifting into plasma tails or plasmaspheric bulges and generating the hiss locally. Some drawbacks of conducting statistical studies using Polar data are that the data collected by Polar lasted for only one year (1996 – 1997), which was during solar minimum without intense geomagnetic storms (Tsurutani et al., 2006). The Polar spacecraft also spent only a small fraction of its orbital period near the geomagnetic equator. Van Allen probes, on the other hand, have extensive spatial coverage over the entire inner magnetosphere ($L < 6$) near the geomagnetic equator and thus, the data from these probes are suitable to provide improved statistical results. With this aim, using two years of Van Allen probe data, Li et al. (2015) evaluated the global distribution of plasmaspheric hiss wave power and frequency spectrum for different levels of substorm activity. Statistical evaluation of the global distribution of plasmaspheric hiss waves showed that the hiss wave amplitudes are dependent on substorm activity: stronger (weaker) wave amplitudes occur in association with increased levels of substorm activity on the dayside (nightside). In contrast to the enhancement of plasmaspheric hiss during geomagnetic disturbances, they have also been found to disappear following interplanetary shocks. Su et al. (2015) first reported the disappearance of plasmaspheric hiss for about 5 hours following an IP shock on October 8, 2013. Such disappearance of hiss waves were attributed to enhanced Landau damping of chorus waves by suprathermal electrons, thereby preventing such waves from entering the plasmasphere followed by removal of source electrons for chorus waves by the shrinking magnetopause. Another event of hiss disappearance and recovery following an IP shock on February 27, 2014 was reported by Liu et al. (2017). They concluded that removal of source electrons and insignificant variation of wave instability were the reasons behind the prompt disappearance of plasmaspheric hiss while subsequent substorm injection of hot electrons and enhanced wave instability resulted in its reappearance. Yue et al. (2017) performed a statistical study on modifications of whistler mode waves in response to interplanetary (IP) shocks using both Van Allen Probes and THEMIS data. From a database of 86 IP shocks, they found that for 43 (35%) shocks, the hiss wave power decreased/disappeared, for 36 (29%) shocks, the hiss wave power increased and for 62 (41%) shocks, chorus wave power intensified. They reported that the hiss disappearance events were found mostly on the dayside while the intensification events occurred mostly on the nightside. They also found the hiss wave power to intensify with enhanced solar wind ram pressure which is in agreement with the findings of Tsurutani et al. (2015).

From these studies, it is quite apparent that plasmaspheric hiss waves exhibit complex variability in response to geomagnetic disturbances, although only a few studies have been conducted in the past due to the scarcity of such enhancement/disappearance events and the fortuitous position of satellites at the right location to observe the waves. Thus, to better our understanding, it is necessary to study more plasmaspheric hiss events that in turn will aid us to understand the particle acceleration or precipitation associated with the passage of IP shocks. Towards that goal, we can consider a test case wherein two interplanetary shocks impinge on the magnetosphere in quick succession and study the variability of plasmaspheric hiss under such a situation. On December 19, 2015, two interplanetary shocks impinged on the magnetosphere within an interval of $\sim$2 hours. Both the Van Allen probes were in the right place at the right time to observe the two shock impacts and the variability of plasmaspheric hiss associated with them. Apart from storms and substorms, ULF waves are also known to modulate hiss wave intensities in a significant manner (e.g., Breneman et al. (2015); Shi et al. (2018)). In the present shock event, both the shocks triggered substorms and in addition, the second shock generated ULF waves as well. Thus, this event serves as a perfect test bed to testify all these mechanisms. We used both particle and wave data from the twin Van Allen probes and calculated the electron phase density (PSD) and linear growth rates of whistler mode waves to understand the variability of plasmaspheric hiss during this entire interval.

The organization of this paper is as follows: in Section 2, we provide an overview of the plasmaspheric hiss event followed by the wave propagation characteristics in Section 3. In Section 4, we provide the results from the analyses of the events. Finally, we discuss the results and provide our concluding remarks in Section 5.

2 Event Overview

Figure 1 provides an overview of the plasmaspheric hiss event on December 19, 2015. The solar wind magnetic field **B** (Figure 1a), proton density N_{sw} and flow velocity V_{sw} (Figure 1b) are acquired from the measurements of Magnetic Field Investigation (MFI) and Solar Wind Experiment (SWE) instruments onboard the WIND spacecraft. The geomagnetic indices SYM-H and AL (Figure 1d) are obtained from the World Data Centre for Geomagnetism, Kyoto. All the parameters are time-shifted to the bow shock nose. The magnetopause location L_{mp} (Figure 1c) is calculated from the Lin et al. (2010) statistical model. Figures 1f and 1g show the magnetic field Power Spectral Density (PSD) measured by the Waveform Receiver (WFR) on the Electric and Magnetic Field Instrument Suite and Integrated Science (EMFISIS) (Kletzing et al., 2013) instrument onboard the twin RBSP spacecraft. Plasmaspheric cold electron densities (Figure 1e) are estimated from the spacecraft potentials derived from the V3 and V4 probes of the Electric Fields and Waves (EFW) instrument (Wygant et al., 2013). The two shock arrival times are marked by vertical dashed lines exhibiting steep increases in N_{sw}, V_{sw} (Figure 1b) and P_{dyn} (Figure 1c). After the first shock, clear signatures of the passage of sheath region can be identified by the rapid fluctuations in these parameters, although such features are absent during the second shock. However, considering the abrupt changes in these parameters that characterize an interplanetary shock, we consider both the pressure pulses as shocks in the present case. Both the shocks compressed the magnetosphere and initiated sudden storm commencement events (for the first shock: $\Delta L_{mp} = 4R_E$; ΔSYM-H = 25 nT and for the second shock: $\Delta L_{mp} = 2R_E$; ΔSYM-H = 27 nT). Substorm activities were also triggered after a few minutes of both the shock impacts: the first shock triggered moderate substorm activity ($AL_{min} \approx -700$ nT) while the second shock triggered weak substorm activity ($AL_{min} \approx -500$ nT) (Figure 1d).

Before the arrival of the first shock at 16:16 UT, both the RBSP satellites were inside the dense plasmasphere (the electron density measured by both the probes were close to 100 cm^{-3}; Figure 1e) and were observing substantial plasmaspheric hiss in the frequency range 0.1 – 2 kHz (Figures 1f, 1g). With the arrival of the shock, the hiss waves observed by both the probes disappeared in the frequency range of 0.1 – 1 kHz and weak waves above 1 kHz emerged. After ∼30 minutes of the impact of the shock, strong recovery of plasmaspheric hiss commenced in the core frequency range (0.1 – 0.5 Hz) for both the probes (Figures 1f, 1g), but the hiss wave power observed by the two RBSP satellites exhibited remarkable difference despite the fact that both the probes were close to one another (during this interval, the maximum separation between the two Van Allen probes was 0.06 hrs in MLT, 0.1 R_E in L and 0.83° in MLAT). After ∼17:45 UT (L ∼ 5.99, MLT ∼ 11.65), the wave amplitude recorded by RBSP-B reduced remarkably but RBSP-A continued to observe hiss of considerable intensity up to the arrival of the second shock (L ∼ 5.92, MLT ∼ 11.74) (Figures 1f, 1g).

The second shock arrived at 18:02 UT and during this time, the twin RBSP spacecraft observed intermittent patchy hiss for ∼1 hour following the shock, with the hiss power concentrated around 600 Hz for both the probes (Figures 1f, 1g). For RBSP-A, the significant recovery of hiss began at ∼ 19:15 UT (L ∼ 5.61, MLT ∼ 12.49) while for RBSP-B, the recovery began at ∼18:45 UT (L ∼ 5.67, MLT ∼ 12.25).

Figure 2 gives a zoomed-in view of the hot electron distributions and electromagnetic fields around the shock arrival times. The omnidirectional (Figures 2a, 2e) and differential (Figures 2b, 2f; 2c, 2g) electron fluxes are measured by the Helium Oxygen Pro-

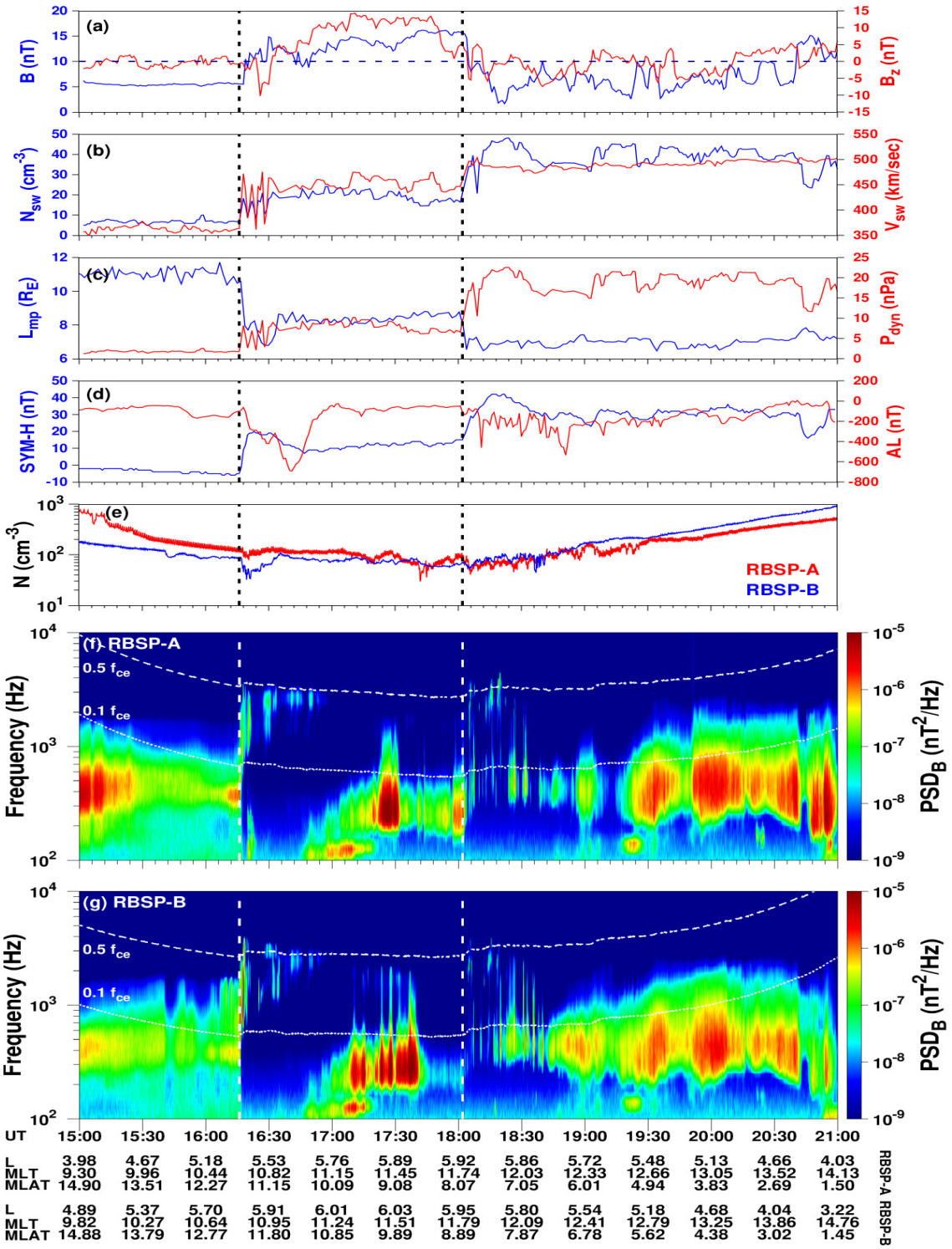

Figure 1. Overview of the plasmaspheric hiss event on December 19, 2015: (a) solar wind magnetic field magnitude (B) and the z-component of the magnetic field (B_z) in GSM coordinates; (b) solar wind proton number density (N_{sw}) and solar wind velocity (V_{sw}); (c) magnetopause location (L_{mp}) and solar wind dynamic pressure (P_{dyn}); (d) geomagnetic activity indices SYM-H and AL; (e) cold electron densities calculated from the EFW probe potentials for RBSP-A (red) and RBSP-B (blue); magnetic field power spectral density (PSD) in the Waveform Receiver (WFR) channels observed by (f) RBSP-A and (g) RBSP-B. The arrival of the two interplanetary shocks are shown by the two vertical dashed lines. The dashed and dotted curves in panels f and g represent $0.5f_{ce}$ and $0.1f_{ce}$ respectively.

ton Electron (HOPE) Mass Spectrometer (Funsten et al., 2013), Magnetic Electron Ion Spectrometer (MagEIS) (Blake et al., 2013) and Relativistic Electron-Proton Telescope (REPT) (Baker et al., 2013) of the Energetic Particle, Composition, and Thermal Plasma (ECT) suite (Spence et al., 2013). The electric and magnetic field measurements (Figures 2d, 2h) are obtained from the EFW and EMFISIS magnetometer (MAG), respectively. With the arrival of the first shock (16:16 UT), the energetic electron fluxes increased followed by a gradual decrease to their pre-shock values (Figures 2a, 2e; 2b, 2f). The relativistic electron fluxes exhibited some additional quasi-periodic fluctuations (Figures 2c, 2g), the duration of which interestingly coincided with the hiss disappearance interval (Figures 1f and 1g). During the intermediate hiss recovery interval (16:45 – 18:02 UT), the energetic electron fluxes began to increase with peaks exhibiting an energy dependent time delay (Figures 2b, 2f) and the hot electron fluxes were significantly enhanced (Figures 2a, 2e). After the second shock (18:02 UT), the energetic electron fluxes exhibited similar trend of initial increase followed by a gradual decrease to their pre-flux levels, but now, quasi-periodic fluctuations were superposed on this general trend, especially at lower MagEIS energy channels (Figures 2b, 2f). Interestingly, these types of fluctuations were also noticed in AL during this time (Figure 1d). For the REPT measured differential electron flux, the second shock did not produce any notable effects (Figure 2c, 2g).

3 Wave Propagation Characteristics

Figure 3 shows the wave propagation characteristics (planarity, ellipticity, wave normal angle and sign of parallel Poynting flux) derived from RBSP observations using the singular value decomposition method (Santolík et al., 2003). During the entire period of our study, the hiss waves had high planarity values ($\sim> 0.5$) (Figures 3b, g). The hiss waves during the intermediate recovery phase (16:45 – 18:02 UT) had the largest values of planarity (0.7 – 1) followed by the pre-shock hiss (0.5 – 0.7). The waves were whistler mode waves with ellipticity values close to 1 (Figures 3c, h). The wave normal angle was less than 20° during the entire period of study (Figures 3d, i). This suggests that the wave propagation direction was almost parallel to the ambient magnetic field. From Figure 1e, we can see that before the arrival of the first shock (15:00 – 16:16 UT) and during the substantial hiss recovery phase (19:00 – 21:00 UT), the Van Allen probes were inside the plasmasphere. The hiss waves during these periods exhibited unidirectional Poynting fluxes which implies that the waves might be generated by local plasma instability at the equator and then subsequent propagation to higher latitudes (Thorne et al., 1979; Laakso et al., 2015; Omura et al., 2015). In the intermediate interval (16:16 – 19:00 UT), the two probes were mostly in the outer plasmasphere and encountered a fluctuating plasmapause location manifested as fluctuations in the measured electron density. During this period, the hiss waves exhibited bidirectional Poynting fluxes which implies additional contribution from embryonic source like chorus waves to the generation of hiss (Bortnik et al., 2008, 2009, 2011; Chen et al., 2012a, 2012b).

4 Data Analyses and Results

The two most accepted mechanisms of plasmaspheric hiss generation below 1 kHz, containing most of the hiss wave power, are: (1) in-situ amplification of hiss inside the plasmasphere by electron cyclotron instability (Thorne et al., 1979; Summers et al., 2014) and (2) generation of incoherent hiss by refraction of chorus waves from a source region outside the plasmasphere to inside of it (Bortnik et al., 2008; Chen et al., 2012b), or some combination of the two. The first mechanism is primarily governed by plasmaspheric electron distributions while the second mechanism depends on the plasmatrough electron distribution.

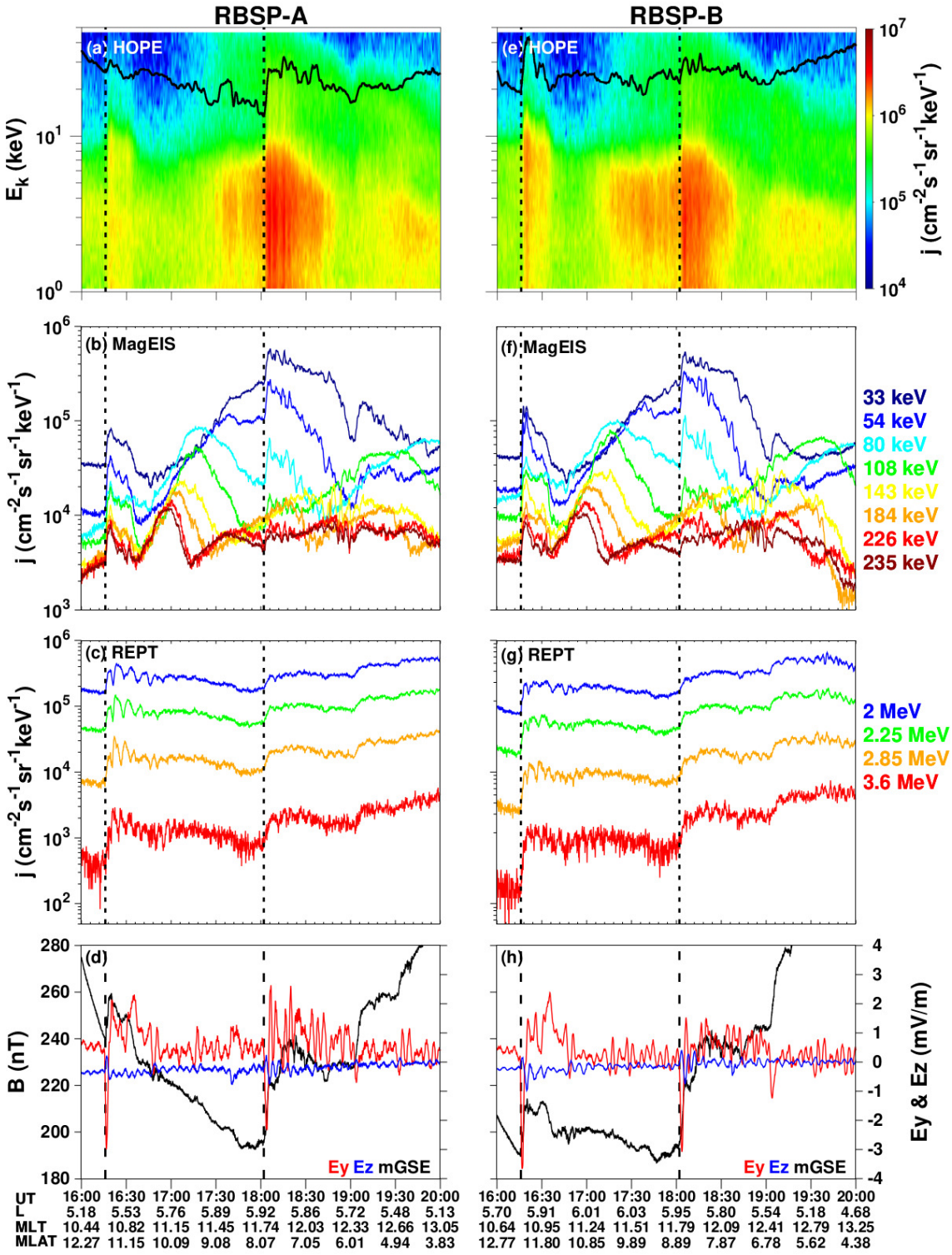

Figure 2. RBSP observation of: (a, e) omnidirectional and (b, f; c, g) unidirectional electron fluxes; and (d, h) electromagnetic fields observed by EMFISIS magnetometer and EFW instruments on December 19, 2015. The two vertical dashed lines mark the arrival of the two interplanetary shocks. The black solid lines in panels (a) and (e) represent the minimum resonant energies (E_{min}) of 0.35 kHz whistler-mode waves.

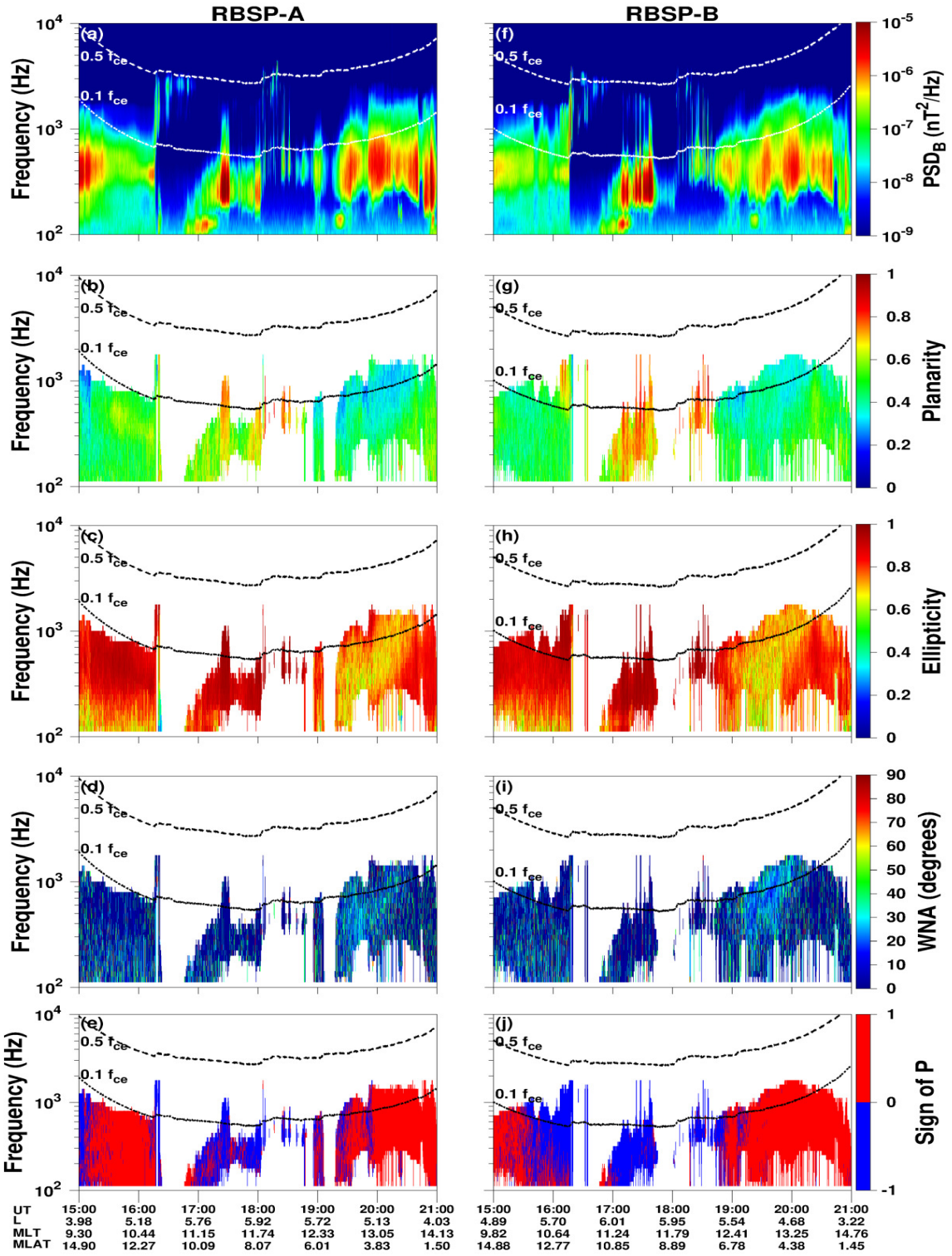

Figure 3. Wave propagation characteristics measured by RBSP-A (a – e) and RBSP-B (f – j) on December 19, 2015: (a, f) magnetic field power spectral density (PSD); (b, g) planarity; (c, h) ellipticity; (d, i) wave normal angle (WNA); (e, j) sign of parallel Poynting flux. The dashed and dotted curves represent $0.5f_{ce}$ and $0.1f_{ce}$ respectively.

Figures 2 (a–c, e–g) give an overview of the hot electron distributions in response to the two shocks. Both the shocks caused prompt enhancements of electron fluxes over a wide range of energies. Induced electric field after the passage of an IP shock can energize electrons through drift-resonance mechanism (e.g., Blake et al. (1992); Foster et al. (2015); Su et al. (2015)). Figures 2d and 2h show that after the passage of both the shocks, the azimuthal component of the electric field (E_y) exhibited bipolar variations while after the second shock, it exhibited additional quasi-periodic fluctuations with peak amplitudes of 3 mV/m. These strong electric field oscillations may have resulted in the energization/acceleration of the hot electrons and thus, caused the electron flux to increase by up to 10 times following the shocks. The minimum resonant energy E_{min} of parallel-propagating whistler mode waves (Meredith et al., 2003) at 350 Hz (frequency of observed maximum hiss intensity) varied between 10 – 40 keV during the period of our interest (Figures 2a, 2e). Before the arrival of the first shock, suprathermal electron fluxes above E_{min} were considerably low. With the arrival of the shock, the suprathermal electron fluxes were initially enhanced which were gradually removed probably through magnetopause shadowing process due to the earthward compression of the magnetosphere. With time, the moderate substorm that was triggered by the first shock injected hot electrons into the inner magnetosphere. This resulted in the gradual enhancement of suprathermal electron fluxes above E_{min}. Such flux enhancements can also be seen to exist during the second shock. The effect of such enhancements is likely to promote local wave instability favoring the growth of whistler mode waves.

Whistler mode waves, including hiss, experience Landau damping/cyclotron resonant amplification by the suprathermal electrons in the course of its propagation. So, to understand the observed wave amplitude variability, we computed the linear growth rates of whistler mode waves. For this, first we calculated the pitch angle distribution of energetic electron phase space density (PSD) from RBSP-A observations and fit these observed PSDs by a distribution function having the form of a sum of subtracted Maxwellian components (Ashour-Abdalla & Kennel, 1978). The fitting parameters (listed in Table 1) are then incorporated into the Waves in Homogeneous Anisotropic Magnetized Plasma (WHAMP) code (Ronmark, 1982) to calculate the linear growth rates of parallel propagating whistler mode waves. Hiss wave normal angle (WNA) is a very important parameter for studying radiation belt dynamics (Meredith et al., 2007; Ni et al., 2014). Statistical results have shown that equatorial hiss WNAs ($|\text{MLAT}| \leq 10^\circ$) are less than or equal to 30°, while mid-latitude hiss WNAs ($|\text{MLAT}| \geq 10^\circ$) are mostly larger than 30° for regions inside the plasmasphere ($L \leq 5$) (Yu et al., 2017). In our case, both the probes were in low latitude plasmasphere ($|\text{MLAT}| \leq 12^\circ$; $L \leq 6$) and from Figures 3d and 3h, we can see that the hiss WNAs were $\leq 20^\circ$ for the entire period of our study. Therefore, the approximation of parallel propagation has been applied for calculations.

Figures 4a – 4g show the observed (filled circles) and fitted (solid lines) plasmaspheric hot electron PSD at the color coded energies at seven specific times: (a) pre-shock (16:00 UT), (b, c) post (first) shock (16:20 UT and 16:40 UT, respectively), (d) intermediate hiss recovery (17:30 UT), (e, f) post (second) shock (18:07 UT and 18:09 UT, respectively) and (g) substantial hiss recovery (20:00 UT). We can see good agreement between the observed and fitted PSDs. Also, the electron PSD increased significantly after the shock impacts with clear pitch angle anisotropies. The distribution function has the form:

$$F(v_\perp, v_\parallel) = \sum_{i=1}^{N} F_i, \tag{1}$$

where,

$$F_i = \frac{n_i}{(\sqrt{\pi}V_{th_i})^3}\exp\left[-\left(\frac{v_{\parallel}}{V_{th_i}}-V_{dr_i}\right)^2\right]\times\left\{\frac{\Delta_i}{\alpha_{1_i}}\exp\left(-\frac{v_{\perp}^2}{\alpha_{1_i}V_{th_i}^2}\right)+\frac{1-\Delta_i}{\alpha_{1_i}-\alpha_{2_i}} \times\left[\exp\left(-\frac{v_{\perp}^2}{\alpha_{1_i}V_{th_i}^2}\right)-\exp\left(-\frac{v_{\perp}^2}{\alpha_{2_i}V_{th_i}^2}\right)\right]\right\}. \quad (2)$$

Here, we have taken $N = 6$ plasma components. At a particular moment, for the ith component, n_i is the density (m^{-3}), $V_{th_i} = \sqrt{2T_i/m_e}$ is the field-aligned thermal velocity, V_{dr_i} is the normalized drift velocity, α_{1_i} and α_{2_i} represent the temperature anisotropy and the size of loss cone respectively, and Δ_i denotes the depth of the loss cone.

In Table 1, we have listed the fitting parameters at seven specific times as mentioned above. The six plasma components corresponding to a particular time instant refer to the plasmaspheric hot electron densities having different plasma parameters. The cold electron densities were procured from RBSP observations. They were calculated by subtracting the hot electron densities (listed in Table 1) from the total electron density observed by both the probes. To calculate the growth rates of whistler waves using WHAMP code, we need to maintain charge neutrality. To satisfy this condition, we considered protons with equal density as the total plasmaspheric electron density (sum of the hot and cold electron densities). This complete set of parameters finally gave the linear growth rate at a particular time instant. Growth rates at other time instants were obtained by following the same above-mentioned steps at the respective moments.

Figure 4h shows the linear growth rates of parallel propagating whistler mode waves at the specified times used in Figures 4 (a – g). Now, let us individually investigate the five hiss intervals to understand the observed hiss variability.

4.1 Pre-shock phase (15:00 UT – 16:16 UT)

Before the arrival of the first shock, the magnetosphere was in a relatively quiet state (Figures 1a – 1d). Both the RBSP satellites were inside the dense plasmasphere (Figure 1e) and were observing plasmaspheric hiss waves in the frequency range 0.1 – 2 kHz (Figure 1f, 1g). The linear growth rate of hiss waves at 16:00 UT peaked at ∼1 kHz (Figure 4h) justifying the observation of hiss in this frequency range. The hiss waves also exhibited unidirectional Poynting fluxes during this interval (Figure 3e). The generation of hiss during this interval thus seems to be a result of the local processes inside the plasmasphere (e.g., Omura et al. (2015); Thorne et al. (1979); Laakso et al. (2015)).

4.2 Post first shock phase (16:16 UT – 16:45 UT)

The first shock did not enhance the growth rate of whistler mode waves in the core frequency range of plasmaspheric hiss. Significant Landau damping by suprathermal electrons can suppress the hiss wave amplitude (Su et al., 2015) that might play a role in removing any pre-existing hiss emissions. From Figure 4b, we find that the electron PSD at 16:20 UT was much higher than the pre-shock values. The linear wave growth rate at this moment peaked at ∼1.5 kHz (Figure 4h). Thus, the enhanced suprathermal electrons may have caused damping of the hiss waves at this moment. After the initial enhancement, the suprathermal electron fluxes above E_{min} were largely depleted (Figure 2a), the consequences of which is likely to oppose the local generation of hiss inside the plasmasphere. We calculated the pitch angle distribution of electron PSD (Figure 4c) and the linear wave growth rate (Figure 4h) at a later time (16:40 UT) when the suprathermal electron fluxes were reduced to almost the preshock levels. The linear wave growth rate calculated at this moment also showed no enhancement within the core frequency range of plasmaspheric hiss and peaked at ∼1.3 kHz. Thus the conditions during this interval became unfavorable for the generation of hiss. This explains the quenching of

Table 1. Fitting parameters for calculating electron PSDs at seven specific times

Epochs	Components	$n_i(m^{-3})$	$T_i(keV)$	Δ_i	α_{1_i}	α_{2_i}	V_{dr_i}
Preshock	1	2.50×10^4	0.1500	0.8	1.0779	0.1078	0
16:00 UT	2	1.76×10^4	1.7200	0.8	1.1952	0.1212	0
	3	1.00×10^4	4.1572	0.8	1.2834	0.1272	0
	4	1.00×10^3	4.9462	0.8	1.2521	0.1250	0
	5	6.76×10^2	12.9779	0.8	1.2800	0.2280	0
	6	3.92×10^2	30.784	0.8	1.1500	0.1150	0
Post first	1	9.37×10^5	0.1260	0.8	1.5758	0.1576	0
shock	2	2.50×10^5	1.2774	0.8	1.3721	0.1372	0
16:20 UT	3	8.27×10^3	3.4057	0.8	1.6722	0.1672	0
	4	7.27×10^3	5.2779	0.8	1.4247	0.1425	0
	5	2.87×10^3	9.8682	0.8	1.0100	0.1010	0
	6	8.25×10^2	30.988	0.8	1.400	0.140	0
Post first	1	1.37×10^5	0.0126	0.8	1.5758	0.1576	0
shock	2	6.50×10^4	1.2774	0.79	1.3721	0.1372	0
16:40 UT	3	6.27×10^3	2.4057	1.0	1.9722	0.1972	0
	4	4.27×10^3	4.2779	0.8	1.1247	0.1125	0
	5	8.87×10^2	6.8682	0.87	1.2500	0.0125	0
	6	7.25×10^2	29.988	0.8	1.1100	0.1110	0
Intermediate	1	2.00×10^4	0.0126	0.8	1.0758	0.1076	0
hiss recovery	2	1.10×10^4	1.1774	0.8	1.1721	0.1172	0
17:30 UT	3	6.55×10^3	1.2257	0.75	1.2722	0.1272	0
	4	5.30×10^3	6.7779	0.75	1.1347	0.1325	0
	5	2.97×10^3	16.8682	0.8	1.1700	0.1170	0
	6	2.95×10^3	18.955	0.8	1.2000	0.1200	0
Post second	1	7.00×10^4	0.0126	0.8	1.0758	0.1076	0
shock	2	5.80×10^4	1.3274	0.8	1.0111	0.1011	0
18:07 UT	3	4.75×10^4	6.6257	0.75	1.2722	0.1272	0
	4	8.30×10^3	8.7779	0.75	1.4347	0.1435	0
	5	4.97×10^3	9.2682	0.8	1.1700	0.1170	0
	6	4.95×10^2	32.955	0.8	1.6000	0.1600	0
Post second	1	1.00×10^4	0.0100	0.8	1.0258	0.1026	0
shock	2	1.00×10^4	2.3274	0.8	1.3111	0.1311	0
18:09 UT	3	1.00×10^4	9.6257	0.8	1.3722	0.1372	0
	4	6.30×10^3	8.7779	0.8	1.4347	0.1435	0
	5	2.97×10^3	9.2682	0.8	1.0100	0.1010	0
	6	4.95×10^2	28.955	0.8	1.6000	0.1600	0
Substantial	1	4.50×10^4	0.1500	0.8	1.0779	0.1078	0
hiss recovery	2	3.90×10^4	1.7200	0.8	1.2121	0.1212	0
20:00 UT	3	1.00×10^4	4.1572	0.8	1.2725	0.1272	0
	4	1.00×10^3	10.8779	0.8	1.4500	0.1450	0
	5	9.77×10^2	24.7682	0.9	1.2800	0.2280	0
	6	7.92×10^2	26.80	0.9	1.2000	0.1200	0

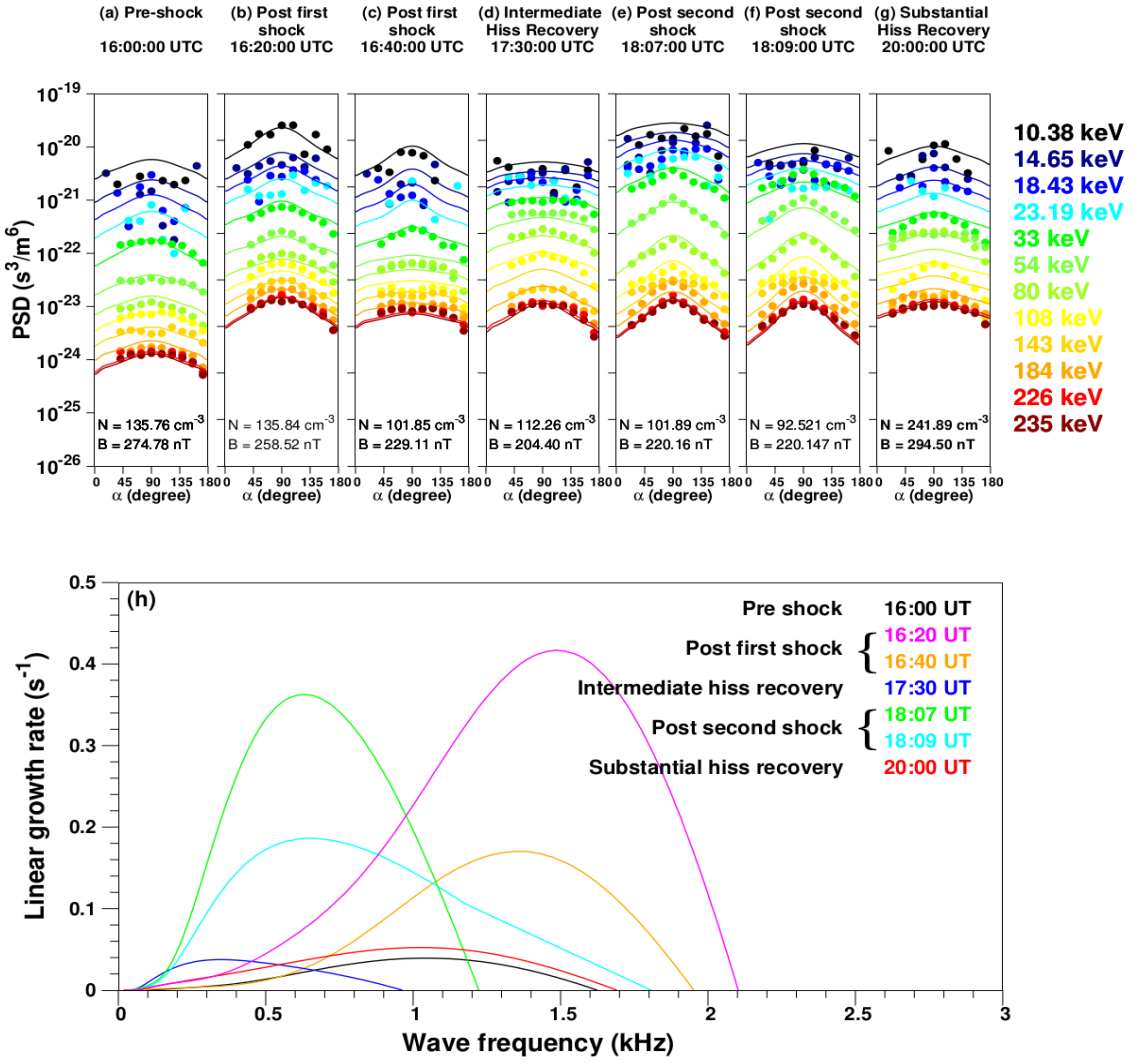

Figure 4. (a – g) Energetic electron (color coded: 10.38 keV – 235 keV) pitch angle distribution of phase space densities (PSD): circles corresponding to RBSP-A observations and solid lines corresponding to their fittings using the distribution function (1); (h) linear growth rate of parallel propagating whistler mode waves corresponding to the times in panels (a – g).

the waves below 1 kHz and the generation of weak whistler waves above 1 kHz following the shock.

4.3 Intermediate hiss recovery phase (16:45 UT – 18:02 UT)

During this interval, the suprathermal electron fluxes were significantly enhanced above E_{min} (Figure 2a), possibly due to the injection of hot electrons into the inner magnetosphere by the moderate substorm activity ($AL_{min} \approx -700$ nT) that was triggered by the first shock. The effect of such flux enhancement is likely to amplify the local instabilities which in turn will favor the growth of whistler waves. The linear growth rate at 17:30 UT peaked in the core frequency range at ∼350 Hz (Figure 4h) that supports this proposition. The spacecraft at this moment moved close to the plasmapause and encountered a partially eroded plasmasphere as evident from the rapid fluctuations in the

measured electron density (Figure 1e). The hiss waves also exhibited bidirectional Poynting fluxes during this interval (Figure 3e). Therefore, the strong intermediate recovery of plasmaspheric hiss waves can be possibly attributed to a combined effect of local plasma instability driven by an inhomogeneous spatial distribution of hot electrons injected by the substorm and an embryonic source such as the chorus waves. Unfortunately, lack of observations at regions outside the plasmasphere from other satellites like THEMIS restrict us to examine the direct chorus-to-hiss mechanism during this event.

4.4 Post second shock phase (18:02 UT – 19:00 UT)

The second shock initiated a weak substorm with $AL_{min} \approx -400$ nT. The suprathermal electron fluxes were already enhanced by the first shock-induced substorm during this period. The substorm triggered by the second shock further increased the fluxes (Figures 2a, 2e). This is evident from Figures 4e and 4f, where we can see that the electron PSD increased considerably during this period. As discussed before, such flux enhancement is likely to facilitate the local growth of whistler mode waves. From the calculation of the linear growth rate during this interval, it was found to increase within the apparent frequency range of plasmaspheric hiss peaking at ∼700 Hz (Figure 4h). The growth rate during this period were also considerably high that might have helped the hiss waves to overcome any suprathermal damping. This explains the occurrence of hiss in the frequency range 0.3 – 1 kHz during this period. The hiss waves also exhibited bidirectional Poynting fluxes (Figure 3e) suggestive of both local in-situ generation and possible additional contribution from embryonic chorus waves to the generation of hiss during this interval. ULF oscillations in E_y might have imposed additional effects generating intermittent wave intensities.

ULF waves are mostly generated by interactions between transient solar wind pressure changes associated with interplanetary shocks and the magnetosphere (Yang et al., 2008; X. Y. Zhang et al., 2009) while they are also known to be internally generated by plasma instabilities and substorms (Ozeke & Mann, 2008; Bentley et al., 2018). These waves can modulate energetic electron fluxes, typically through drift resonance (Southwood & Kivelson, 1981) which in turn can modulate the hiss wave intensities. Figures 2d and 2h show the electric field measurements from EFW instruments (plotted after taking a 100-second running average to minimize the noise in the data) and the magnetic field measurements from EMFISIS magnetometer instruments. Following both the shocks, E_y exhibited bipolar variations while after the second shock impact, additional strong ULF oscillations in E_y can be clearly seen.

To analyze the potential role of these quasi-periodic oscillations on hiss wave amplitude modulation, the electric and magnetic fields were rotated into a mean field-aligned (MFA) coordinate system (Takahashi et al., 1990), determined by 400 sec sliding average of EMFISIS and EFW data. This helped to detect the dominant mode of fluctuation in the magnetic field as poloidal (radial), toroidal (azimuthal) or compressional (parallel). Residual electron flux, defined as $\frac{J-J_0}{J_0}$, where J is the observed electron flux at a particular MagEIS energy channel and J_0 is a 10 minute, running boxcar average of J (Claudepierre et al., 2013) was calculated to analyze the electron flux variations. From Figures 5(a – c, f – h), we can see strong oscillations in the radial component of the magnetic field (B_r) and azimuthal component of the electric field (E_a) compared to B_a and E_r, while the parallel component of the magnetic field (B_p) show irregular variations with very poor periodicity. Moreover, as fundamental mode ULF waves are known to modulate energetic electrons significantly (Q. Zong et al., 2011) and in our case, we found the energetic electron fluxes to be significantly modulated by the ULF waves, it is indicative that the ULF waves generated by the second shock are fundamental harmonic poloidal Pc5 mode (periodicity ∼240 sec) waves. Further, we can see $\sim 90^\circ$ phase difference between B_a and E_r (for the first few wave cycles) indicating a standing mode wave. This suggests that the transverse waves detected satisfied Field Line Resonance

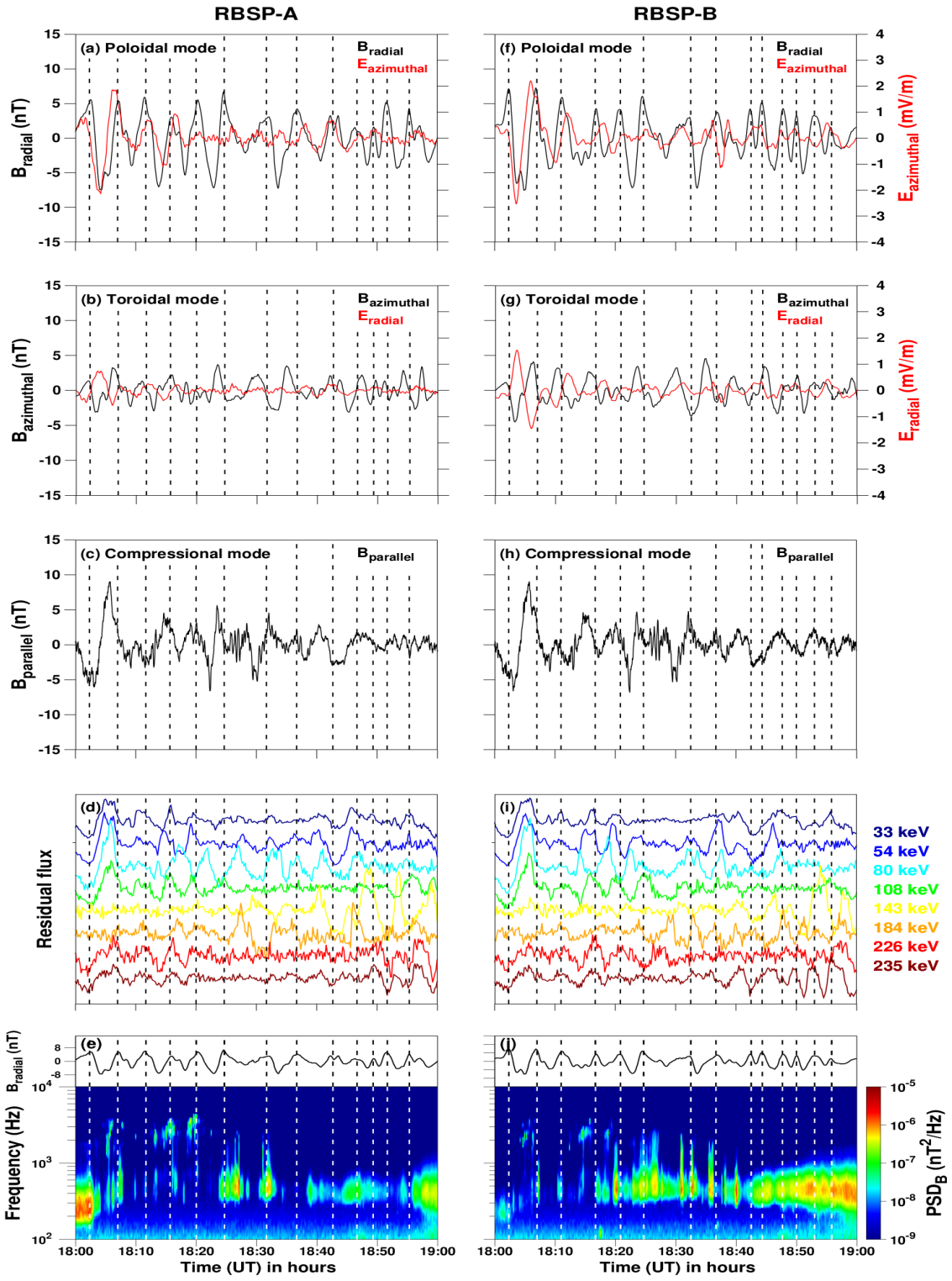

Figure 5. (a – c, f – h) Radial, azimuthal and compressional components of the electromagnetic field measured by EFW and EMFISIS instruments presented in MFA coordinates. (d, i) Residual electron flux $\frac{J-J_0}{J_0}$. (e, j) Magnetic field PSD in the WFR channels and the B_{radial} curves of panels a and f. The vertical dashed lines mark the quasi-periodic variations of the poloidal mode.

(FLR) condition. IP-shock induced ULF waves are suggested to be excited through the FLR mechanism (e.g., Araki et al. (1997); Chi et al. (2001); Sarris et al. (2010); X. Y. Zhang et al. (2010); Q.-G. Zong et al. (2009); D. Zhang et al. (2020)). As the interplanetry shock hits the magnetopause, it causes a global compression of the dayside magnetosphere that launches tailward propagating fast-mode waves. These waves propagate into the magnetosphere and excite field line resonance (FLR). Thus, the ULF waves after the second shock might be generated by this FLR mechanism.

One criterion for occurrence of wave-particle drift resonance is that the resonant particle flux should oscillate either in phase or anti-phase with E_a while non-resonant particle fluxes should oscillate 90° out of phase with E_a (Southwood & Kivelson, 1981; Dai et al., 2013). Similarly, the resonant energy can also be determined by examining the flux peak to valley ratio γ (Yang et al., 2010). γ of electron fluxes in the resonant energy range would be larger than the adjacent energies. Both these features are clearly visible for electrons in the energy range 80 – 108 keV for the first 6 wave cycles (the vertical dashed lines in Figure 5 representing the quasi-periodicity of the poloidal mode). Residual fluxes at other electron energies exhibit weak correlation with the magnetic field pulsations. Thus, the drift resonance must have been excited in the 80 – 108 keV energy channel. Although at other energies the electrons do not exhibit exact drift resonance with the ULF waves, their modulations are highly pertinent to the presence of ULF waves. Acceleration during the first half cycle followed by deceleration may not have led to any energy gain of these electrons (Shi et al., 2018).

The correlation of ULF waves and hiss intensity modulation is shown in Figures 5e and 5j. The hiss wave intensity exhibits a strong coherency with B_r for the first 6 wave cycles: the intensity peaking at the crest of the magnetic field variations while diminishing or vanishing at its trough. The linear wave growth rates calculated at these intervals also exhibit similar variations. At 18:07 UT (hiss intensity peak), the maximum growth rate was found to be higher than at 18:09 UT (hiss intensity trough) (cf. Figure 3g). At other resonant wave cycles, similar variations of wave growth rates were also found (not shown here to maintain brevity) that justify the observed hiss intensity variations. Such correlation is found to be better for RBSP-A than for RBSP-B. Similar better agreement between electron flux modulations and ULF waves are also observed for RBSP-A compared to RBSP-B. One possible explanation is that the excitation of ULF waves and its modulation of electron flux and hiss wave intensity might have occurred at or near the location of RBSP-A. During propagation from the source region to the location of RBSP-B, the electrons might have become incoherent as their drift motion is dominated by the $\mathbf{E} \times \mathbf{B}$-drift. The waves, on the other hand, might have been affected by the background plasma density.

The analyses, thus suggest that an enhanced growth rate and additional ULF wave modulation triggered the generation of hiss waves during this period.

4.5 Substantial hiss recovery phase (19:00 UT – 21:00 UT)

During this interval, the growth rate (20:00 UT) exhibited similar variations as that of the pre-shock moment (16:00 UT), with the post-shock values higher than the pre-shock values (Figure 4h). The ULF waves excited by the second shock impact subsided and the suprathermal electron fluxes were comparably reduced, although higher than the pre-shock fluxes (Figure 2a). The twin Van Allen probes were also in the dense plasmasphere during this period (Figure 1e) and the hiss waves exhibited unidirectional Poynting fluxes (Figure 3e). Thus, the background magnetospheric conditions became similar to some extent to that during the pre-shock interval. Therefore, as discussed earlier, the local plasma instabilities might have led to the substantial recovery of plasmaspheric hiss during this interval.

5 Discussion and Conclusion

In this study, using RBSP observations and calculation of electron phase space density (PSD) and wave growth rates based on linear instability theory (Kennel & Petschek, 1966), we investigated the mechanisms that caused disappearance, recovery and patchiness of plasmaspheric hiss in response to two consecutive interplanetary shocks on December 19, 2015. Suprathermal damping of hiss waves followed by the removal of hot electrons led to the ∼30 minutes disappearance of plasmaspheric hiss following the first shock (16:16 – 16:45 UT). With time, as more and more hot electrons were injected into the inner magnetosphere by the first shock-induced substorm, the hiss waves recovered within their core frequency range (16:45 – 18:02 UT). Additionally, chorus waves were also found to possibly contribute to the generation of hiss during this interval. Weak substorm activities and Pc5 mode poloidal ULF waves triggered by the second shock resulted in the generation and intermittent variation of plasmaspheric hiss for about an hour following the shock impact (18:02 – 19:00 UT). Afterwards, as the Van Allen probes moved inside the plasmasphere, local plasma instability led the hiss waves to regain their ambient intensity.

The energetic and relativistic electrons were found to exhibit significant variations around the shock arrival times (Figure 2). As discussed in details in Section 1, plasmaspheric hiss waves are particularly important in radiation belt studies as they play vital roles in modulating the radiation belt electron distribution. Recently, numerous studies have been conducted to study the evolution of plasmaspheric electron lifetimes with geomagnetic activity based on hiss power variations with AE or Kp using the Van Allen Probes observations (Spasojevic et al., 2015; Orlova et al., 2016; Mourenas et al., 2017; Claudepierre et al., 2020). Agapitov et al. (2020) used six years of Van Allen probe data (2012 – 2018) to study the plasmaspheric hiss-driven pitch-angle diffusion rates of MeV electrons as a function of L^*, MLT and AE. They considered the local hiss wave power, ratio of electron plasmafrequency to electron gyrofrequency (ω_{pe}/Ω_{ce}), hiss frequency (f_m) at peak hiss power and took into account the spatio-temporal correlation between these parameters to provide comprehensive statistical maps of the diffusion rates. Using a parametric model of MeV electron lifetime governed by AE-index for regions with $L > 2.5$ up to the plasmapause and validated by MagEIS electron flux decay database, it was found that during active geomagnetic intervals, as the hiss wave power and peak wave frequency changes, it reduces the MeV electron lifetimes by ∼1.5 – 2 times, resulting in faster electron precipitation into the atmosphere. This suggests that the distribution of MeV electrons in the plasmasphere can be modulated by plasmaspheric hiss waves, which itself varies with geomagnetic activities. During the period of our study, we found the MeV electron fluxes to exhibit initial enhancement followed by quasi-periodic fluctuations after the first shock impact and after the second shock impact, the fluxes exhibited slight increase in their values that remained elevated above the pre-shock levels for the rest of the period (Figures 2c and 2g). It was also during these intervals that the hiss waves exhibited dramatic variations: disappearing for about 30 minutes after the first shock and exhibiting intermittent patchy variations after the second shock (Figures 1f and 1g). Thus, it seems that apart from shock acceleration (e.g., Blake et al. (1992); Foster et al. (2015); Kanekal et al. (2016)), the plasmaspheric hiss waves might have also played a role in modulating the MeV electron fluxes (e.g., Agapitov et al. (2020); Claudepierre et al. (2020)). However, this requires further investigation that is not in the scope of this present work and so, we leave it for future studies.

In addition to these features in the measured hiss wave amplitude and electron flux distributions, we also observed some differences in the wave amplitudes between the two probes during the interval 16:16 UT – 19:00 UT (mentioned in Section 2). From Figure 1e, we can see that during the pre-shock interval (15:00 UT – 16:16 UT) and the substantial hiss recovery phase (19:00 UT – 21:00 UT), the measured plasmaspheric electron density exhibited smooth variations, but between 16:16 UT – 19:00 UT, the elec-

tron density exhibited constant fluctuations. Chen et al. (2012a), through ray tracing technique, showed that whistler mode waves, including hiss, are focused by density enhancements with larger intensity in regions of higher plasma density. Thus, it is suggestive that consistent density fluctuations along the trajectory of the satellites can lead to sudden increase or decrease in the hiss wave amplitude. To check the role of background plasma density on the observed hiss wave amplitude variations, we over-plotted the plasmaspheric electron density (multiplied by 10 to match the scale) estimated from EFW spacecraft potentials on the magnetic field power spectral density (Figure 6). The figure shows that the hiss wave amplitudes exhibit good correlation with the plasmaspheric density, especially during the intermediate and post second shock intervals.

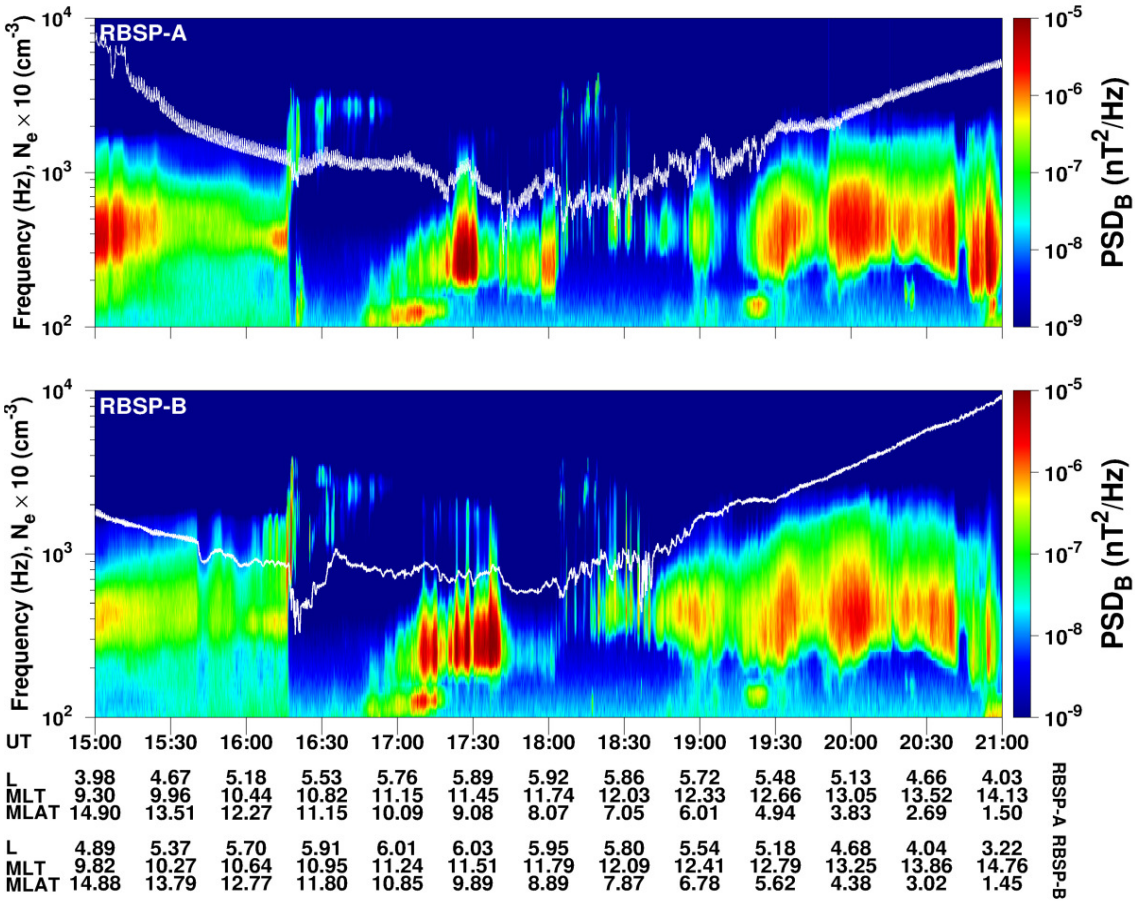

Figure 6. Plasmaspheric electron density estimated from EFW probe potentials (multiplied by 10 to match the scale) shown by white solid lines over-plotted on the magnetic field power spectral density (PSD) in the WFR channels observed by RBSP-A (top panel) and RBSP-B (bottom panel).

Malaspina et al. (2016, 2017), using almost 3 years of Van Allen probe data, presented statistical distribution of hiss wave power with: (1) distance from the plasmapause and (2) location of the plasmapause, rather than the general trend of organizing hiss wave power by L parameter and geomagnetic activity. They argued that as the growth and evolution of whistler mode waves strongly depend on plasmaspheric density distribution that itself varies with L and depends on the history of corotation, convection and refilling, so when the hiss wave power is organized by L parameter and geomagnetic activ-

ity, it introduces non-physical spatial averaging of hiss power distributions. Under this background, distance from the plasmapause and the plasmapause location are better parameters for statistically parameterizing hiss wave power spatial distribution in the inner magnetosphere. Their studies showed that both the location and the width of peak hiss intensity exhibits significant variation with the plasmapause location. The location of peak hiss intensity shifts earthwards to lower L values and the width increases as the plasmapause moves away from the Earth. The location of the plasmapause can be estimated from the plasma density measured by a spacecraft. It is usually defined as the time when the plasma density changes by a factor of $\sim$5 within $\sim$0.5 L (Moldwin et al., 2002). From Figure 1e, we can see that neither of the spacecraft exhibited such sharp changes in the measured electron density. Thus, identification of a true plasmapause crossing is difficult during the period of our study, although consistent fluctuations in the electron density between 16:16 UT – 19:00 UT (Figure 1e) are indicative of a partially eroded plasmasphere and a constantly fluctuating plasmapause location. The observed hiss wave amplitude variations and the differences in wave power measurements between the two probes during this interval (16:16 – 19:00 UT) might thus be effects of the fluctuating plasmapause. Therefore, we see that the fluctuating plasmapause location and in turn, the background plasma density played important roles in modulating the hiss wave power, while substorms and ULF waves resulted in the excitation of the waves.

The main conclusions from this study can thus be summarized as follows:

1. Substorms induced by both the shocks played vital roles in modulating the hiss wave intensities. By injecting hot electrons into the inner magnetosphere, the substorms initiated plasma instabilities that affected the linear wave growth rates leading to the observed hiss variations during these intervals.
2. ULF waves generated by the second shock modulated both the electron fluxes and the hiss wave intensities in a significant manner. Electrons in the energy range 80 – 108 keV were in drift resonance with the ULF waves that resulted in the observed quasi-periodic fluctuations in the electron fluxes. The ULF waves also modulated the hiss wave intensities.
3. Background plasma density and fluctuating plasmapause location additionally played vital roles in modulating the hiss wave intensities during the interval 16:16 UT – 19:00 UT.

In future, we plan to use extensive multi-satellite observations and numerical simulations to understand the variability of plasmaspheric hiss under various and more complex shock impact scenarios.

Acknowledgments

The interplanetary parameters and geomagnetic indices were obtained from the websites (https://wind.nasa.gov/data.php for WIND and http://wdc.kugi.kyoto-u.ac.jp/wdc/Sec3.html for geomagnetic indices). The RBSP data used in this study are available at the websites (http://emfisis.physics.uiowa.edu/Flight/ for EMFISIS, http://www.rbsp-ect.lanl.gov/data_pub/ for ECT, and http://www.space.umn.edu/rbspefw-data/ for EFW). The authors thank Z. P. Su for his help. This work is supported by the Department of Space, Government of India.

References

Agapitov, O., Artemyev, A., Krasnoselskikh, V., Khotyaintsev, Y. V., Mourenas, D., Breuillard, H., ... Rolland, G. (2013). Statistics of whistler mode waves in the outer radiation belt: Cluster STAFF-SA measurements. *Journal of Geophysical Research: Space Physics*, *118*(6), 3407-3420. doi:

https://doi.org/10.1002/jgra.50312

Agapitov, O., Mourenas, D., Artemyev, A., Claudepierre, S. G., Hospodarsky, G., & Bonnell, J. W. (2020). Lifetimes of Relativistic Electrons as Determined From Plasmaspheric Hiss Scattering Rates Statistics: Effects of ω_{pe}/Ω_{ce} and Wave Frequency Dependence on Geomagnetic Activity. *Geophysical Research Letters*, *47*(13). doi: https://doi.org/10.1029/2020GL088052

Agapitov, O., Mourenas, D., Artemyev, A., Mozer, F. S., Bonnell, J. W., Angelopoulos, V., ... Krasnoselskikh, V. (2018). Spatial Extent and Temporal Correlation of Chorus and Hiss: Statistical Results From Multipoint THEMIS Observations. *Journal of Geophysical Research: Space Physics*, *123*(10), 8317-8330. doi: https://doi.org/10.1029/2018JA025725

Araki, T., Fujitani, S., Emoto, M., Yumoto, K., Shiokawa, K., Ichinose, T., ... Liu, C. F. (1997). Anomalous sudden commencement on March 24, 1991. *Journal of Geophysical Research: Space Physics*, *102*(A7), 14075-14086. doi: https://doi.org/10.1029/96JA03637

Ashour-Abdalla, M., & Kennel, C. F. (1978). Nonconvective and convective electron cyclotron harmonic instabilities. *Journal of Geophysical Research: Space Physics*, *83*(A4), 1531-1543. doi: 10.1029/JA083iA04p01531

Baker, D. N., Kanekal, S. G., Hoxie, V. C., Batiste, S., Bolton, M., Li, X., ... Friedel, R. (2013). The Relativistic Electron-Proton Telescope (REPT) Instrument on Board the Radiation Belt Storm Probes (RBSP) Spacecraft: Characterization of Earth's Radiation Belt High-Energy Particle Populations. *Space Science Reviews*, *179*(1), 337-381. doi: 10.1007/s11214-012-9950-9

Bentley, S. N., Watt, C. E. J., Owens, M. J., & Rae, I. J. (2018). ULF Wave Activity in the Magnetosphere: Resolving Solar Wind Interdependencies to Identify Driving Mechanisms. *Journal of Geophysical Research: Space Physics*, *123*(4), 2745-2771. doi: 10.1002/2017JA024740

Blake, J. B., Carranza, P. A., Claudepierre, S. G., Clemmons, J. H., Crain Jr., W. R., Dotan, Y., ... Zakrzewski, M. P. (2013). The Magnetic Electron Ion Spectrometer (MagEIS) Instruments Aboard the Radiation Belt Storm Probes (RBSP) Spacecraft. *Space Science Review*, *179*, 383–421. doi: 10.1007/s11214-013-9991-8

Blake, J. B., Kolasinski, W. A., Fillius, R. W., & Mullen, E. G. (1992). Injection of electrons and protons with energies of tens of MeV into L ¡ 3 on 24 March 1991. *Geophysical Research Letters*, *19*(8), 821-824. doi: https://doi.org/10.1029/92GL00624

Bortnik, J., Chen, L., Li, W., Thorne, R. M., & Horne, R. B. (2011). Modeling the evolution of chorus waves into plasmaspheric hiss. *Journal of Geophysical Research: Space Physics*, *116*(A8). doi: 10.1029/2011JA016499

Bortnik, J., Li, W., Thorne, R. M., Angelopoulos, V., Cully, C., Bonnell, J., ... Roux, A. (2009). An Observation Linking the Origin of Plasmaspheric Hiss to Discrete Chorus Emissions. *Science*, *324*(5928), 775–778. doi: 10.1126/science.1171273

Bortnik, J., Thorne, R., & Meredith, N. (2008). The unexpected origin of plasmaspheric hiss from discrete chorus emissions. *Nature*, *452*, 62-66. doi: 10.1038/nature06741

Breneman, A. W., Halford, A., Millan, R., McCarthy, M., Fennell, J., Sample, J., ... Kletzing, C. A. (2015). Global-scale coherence modulation of radiation-belt electron loss from plasmaspheric hiss. *Nature*, *523*, 193-195. doi: 10.1038/nature14515

Chen, L., Bortnik, J., Li, W., Thorne, R. M., & Horne, R. B. (2012b). Modeling the properties of plasmaspheric hiss: 1. Dependence on chorus wave emission. *Journal of Geophysical Research: Space Physics*, *117*(A5). doi: 10.1029/2011JA017201

Chen, L., Thorne, R. M., Li, W., Bortnik, J., Turner, D., & Angelopoulos, V.

(2012a). Modulation of plasmaspheric hiss intensity by thermal plasma density structure. *Geophysical Research Letters*, *39*(14). doi: 10.1029/2012GL052308

Chi, P. J., Russell, C. T., Raeder, J., Zesta, E., Yumoto, K., Kawano, H., ... Moldwin, M. B. (2001). Propagation of the preliminary reverse impulse of sudden commencements to low latitudes. *Journal of Geophysical Research: Space Physics*, *106*(A9), 18857-18864. doi: https://doi.org/10.1029/2001JA900071

Chum, J., & Santolik, O. (2005). Propagation of whistler-mode chorus to low altitudes: divergent ray trajectories and ground accessibility. *Annales Geophysicae*, *23*, 3727-3738.

Claudepierre, S. G., Ma, Q., Bortnik, J., O'Brien, T. P., Fennell, J. F., & Blake, J. B. (2020). Empirically Estimated Electron Lifetimes in the Earth's Radiation Belts: Comparison With Theory. *Geophysical Research Letters*, *47*(3). doi: https://doi.org/10.1029/2019GL086056

Claudepierre, S. G., Mann, I. R., Takahashi, K., Fennell, J. F., Hudson, M. K., Blake, J. B., ... Wygant, J. R. (2013). Van Allen Probes observation of localized drift resonance between poloidal mode ultra-low frequency waves and 60 keV electrons. *Geophysical Research Letters*, *40*(17), 4491-4497. doi: 10.1002/grl.50901

Dai, L., Takahashi, K., Wygant, J. R., Chen, L., Bonnell, J., Cattell, C. A., ... Spence, H. E. (2013). Excitation of poloidal standing AlfvÃ©n waves through drift resonance wave-particle interaction. *Geophysical Research Letters*, *40*(16), 4127-4132. doi: 10.1002/grl.50800

Dunckel, N., & Helliwell, R. A. (1969). Whistler-mode emissions on the OGO 1 satellite. *Journal of Geophysical Research (1896-1977)*, *74*(26), 6371-6385. doi: 10.1029/JA074i026p06371

Foster, J. C., Wygant, J. R., Hudson, M. K., Boyd, A. J., Baker, D. N., Erickson, P. J., & Spence, H. E. (2015). Shock-induced prompt relativistic electron acceleration in the inner magnetosphere. *Journal of Geophysical Research: Space Physics*, *120*(3), 1661-1674. doi: 10.1002/2014JA020642

Funsten, H. O., Skoug, R. M., Guthrie, A. A., MacDonald, E. A., Baldonado, J. R., Harper, R. W., ... Chen, J. (2013). Helium, Oxygen, Proton, and Electron (HOPE) Mass Spectrometer for the Radiation Belt Storm Probes Mission. *Space Science Review*, *179*, 423–484. doi: 10.1007/s11214-013-9968-7

Green, J. L., Boardsen, S., Garcia, L., Taylor, W. W. L., Fung, S. F., & Reinisch, B. W. (2005). On the origin of whistler mode radiation in the plasmasphere. *Journal of Geophysical Research: Space Physics*, *110*(A3). doi: https://doi.org/10.1029/2004JA010495

Hartley, D. P., Kletzing, C. A., Chen, L., Horne, R. B., & SantolÃk, O. (2019). Van Allen Probes Observations of Chorus Wave Vector Orientations: Implications for the Chorus-to-Hiss Mechanism. *Geophysical Research Letters*, *46*(5), 2337-2346. doi: 10.1029/2019GL082111

Kanekal, S. G., Baker, D. N., Fennell, J. F., Jones, A., Schiller, Q., Richardson, I. G., ... Wygant, J. R. (2016). Prompt acceleration of magnetospheric electrons to ultrarelativistic energies by the 17 March 2015 interplanetary shock. *Journal of Geophysical Research: Space Physics*, *121*(8), 7622-7635. doi: 10.1002/2016JA022596

Kennel, C. F., & Petschek, H. E. (1966). Limit on stably trapped particle fluxes. *Journal of Geophysical Research (1896-1977)*, *71*(1), 1-28. doi: 10.1029/JZ071i001p00001

Kletzing, C. A., Kurth, W. S., Acuna, M., MacDowall, R. J., Torbert, R. B., Averkamp, T., ... Tyler, J. (2013). The Electric and Magnetic Field Instrument Suite and Integrated Science (EMFISIS) on RBSP. *Space Science Review*, *179*, 127–181. doi: 10.1007/s11214-013-9993-6

Laakso, H., Santolik, O., Horne, R., Kolmasová, I., Escoubet, P., Masson, A., & Taylor, M. (2015). Identifying the source region of plasmaspheric hiss. *Geo-*

physical Research Letters, *42*(9), 3141-3149. doi: https://doi.org/10.1002/2015GL063755

Li, W., Ma, Q., Thorne, R. M., Bortnik, J., Kletzing, C. A., Kurth, W. S., ... Nishimura, Y. (2015). Statistical properties of plasmaspheric hiss derived from Van Allen Probes data and their effects on radiation belt electron dynamics. *Journal of Geophysical Research: Space Physics*, *120*(5), 3393-3405. doi: 10.1002/2015JA021048

Lin, R. L., Zhang, X. X., Liu, S. Q., Wang, Y. L., & Gong, J. C. (2010). A three-dimensional asymmetric magnetopause model. *Journal of Geophysical Research: Space Physics*, *115*(A4). doi: 10.1029/2009JA014235

Liu, N., Su, Z., Gao, Z., Reeves, G. D., Zheng, H., Wang, Y., & Wang, S. (2017). Shock-Induced Disappearance and Subsequent Recovery of Plasmaspheric Hiss: Coordinated Observations of RBSP, THEMIS, and POES Satellites. *Journal of Geophysical Research: Space Physics*, *122*(10), 10,421-10,435. doi: 10.1002/2017JA024470

Malaspina, D. M., Jaynes, A. N., Boulé, C., Bortnik, J., Thaller, S. A., Ergun, R. E., ... Wygant, J. R. (2016). The distribution of plasmaspheric hiss wave power with respect to plasmapause location. *Geophysical Research Letters*, *43*(15), 7878-7886. doi: https://doi.org/10.1002/2016GL069982

Malaspina, D. M., Jaynes, A. N., Hospodarsky, G., Bortnik, J., Ergun, R. E., & Wygant, J. (2017). Statistical properties of low-frequency plasmaspheric hiss. *Journal of Geophysical Research: Space Physics*, *122*(8), 8340-8352. doi: https://doi.org/10.1002/2017JA024328

Meredith, N. P., Horne, R. B., Glauert, S. A., & Anderson, R. R. (2007). Slot region electron loss timescales due to plasmaspheric hiss and lightning-generated whistlers. *Journal of Geophysical Research: Space Physics*, *112*(A8). doi: https://doi.org/10.1029/2007JA012413

Meredith, N. P., Horne, R. B., Thorne, R. M., Summers, D., & Anderson, R. R. (2004). Substorm dependence of plasmaspheric hiss. *Journal of Geophysical Research: Space Physics*, *109*(A6). doi: 10.1029/2004JA010387

Meredith, N. P., Thorne, R. M., Horne, R. B., Summers, D., Fraser, B. J., & Anderson, R. R. (2003). Statistical analysis of relativistic electron energies for cyclotron resonance with EMIC waves observed on CRRES. *Journal of Geophysical Research: Space Physics*, *108*(A6). doi: 10.1029/2002JA009700

Moldwin, M. B., Downward, L., Rassoul, H. K., Amin, R., & Anderson, R. R. (2002). A new model of the location of the plasmapause: CRRES results. *Journal of Geophysical Research: Space Physics*, *107*(A11). doi: https://doi.org/10.1029/2001JA009211

Mourenas, D., Ma, Q., Artemyev, A. V., & Li, W. (2017). Scaling laws for the inner structure of the radiation belts. *Geophysical Research Letters*, *44*(7), 3009-3018. doi: https://doi.org/10.1002/2017GL072987

Ni, B., Li, W., Thorne, R. M., Bortnik, J., Ma, Q., Chen, L., ... Claudepierre, S. G. (2014). Resonant scattering of energetic electrons by unusual low-frequency hiss. *Geophysical Research Letters*, *41*(6), 1854-1861. doi: https://doi.org/10.1002/2014GL059389

Omura, Y., Nakamura, S., Kletzing, C. A., Summers, D., & Hikishima, M. (2015). Nonlinear wave growth theory of coherent hiss emissions in the plasmasphere. *Journal of Geophysical Research: Space Physics*, *120*(9), 7642-7657. doi: 10.1002/2015JA021520

Orlova, K., Shprits, Y., & Spasojevic, M. (2016). New global loss model of energetic and relativistic electrons based on Van Allen Probes measurements. *Journal of Geophysical Research: Space Physics*, *121*(2), 1308-1314. doi: https://doi.org/10.1002/2015JA021878

Ozeke, L. G., & Mann, I. R. (2008). Energization of radiation belt electrons by ring current ion driven ULF waves. *Journal of Geophysical Research: Space*

Physics, *113*(A2). doi: 10.1029/2007JA012468

Ripoll, J.-F., Santolík, O., Reeves, G. D., Kurth, W. S., Denton, M. H., Loridan, V., ... Turner, D. L. (2017). Effects of whistler mode hiss waves in March 2013. *Journal of Geophysical Research: Space Physics*, *122*(7), 7433-7462. doi: 10.1002/2017JA024139

Ronmark, K. (1982). Waves in homogeneous, anisotropic, multicomponent plasmas. *Technical Report*, *179*(55).

Russell, C. T., Holzer, R. E., & Smith, E. J. (1969). OGO 3 observations of ELF noise in the magnetosphere: 1. Spatial extent and frequency of occurrence. *Journal of Geophysical Research (1896-1977)*, *74*(3), 755-777. doi: 10.1029/JA074i003p00755

Santolik, O., Chum, J., Parrot, M., Gurnett, D. A., Pickett, J. S., & Cornilleau-Wehrlin, N. (2006). Propagation of whistler mode chorus to low altitudes: Spacecraft observations of structured ELF hiss. *Journal of Geophysical Research: Space Physics*, *111*(A10). doi: 10.1029/2005JA011462

Santolík, O., Parrot, M., & Lefeuvre, F. (2003). Singular value decomposition methods for wave propagation analysis. *Radio Science*, *38*(1). doi: https://doi.org/10.1029/2000RS002523

Sarris, T. E., Liu, W., Li, X., Kabin, K., Talaat, E. R., Rankin, R., ... Glassmeier, K.-H. (2010). THEMIS observations of the spatial extent and pressure-pulse excitation of field line resonances. *Geophysical Research Letters*, *37*(15). doi: https://doi.org/10.1029/2010GL044125

Shi, R., Li, W., Ma, Q., Claudepierre, S. G., Kletzing, C. A., Kurth, W. S., ... Wygant, J. R. (2018). Van Allen Probes observation of plasmaspheric hiss modulated by injected energetic electrons. *Annales Geophysicae*, *36*(3), 781–791. doi: 10.5194/angeo-36-781-2018

Southwood, D. J., & Kivelson, M. G. (1981). Charged particle behavior in low-frequency geomagnetic pulsations 1. Transverse waves. *Journal of Geophysical Research: Space Physics*, *86*(A7), 5643-5655. doi: 10.1029/JA086iA07p05643

Spasojevic, M., Shprits, Y. Y., & Orlova, K. (2015). Global empirical models of plasmaspheric hiss using Van Allen Probes. *Journal of Geophysical Research: Space Physics*, *120*(12), 10,370-10,383. doi: https://doi.org/10.1002/2015JA021803

Spence, H. E., Reeves, G. D., Baker, D. N., Blake, J. B., Bolton, M., Bourdarie, S., ... Thorne, R. M. (2013). Science Goals and Overview of the Radiation Belt Storm Probes (RBSP) Energetic Particle, Composition, and Thermal Plasma (ECT) Suite on NASA's Van Allen Probes Mission. *Space Science Review*, *179*, 311–336. doi: 10.1007/s11214-013-0007-5

Su, Z., Zhu, H., Xiao, F., Zheng, H., Wang, Y., Shen, C., ... Wygant, J. R. (2015). Disappearance of plasmaspheric hiss following interplanetary shock. *Geophysical Research Letters*, *42*(9), 3129-3140. doi: 10.1002/2015GL063906

Summers, D., Ni, B., Meredith, N. P., Horne, R. B., Thorne, R. M., Moldwin, M. B., & Anderson, R. R. (2008). Electron scattering by whistler-mode ELF hiss in plasmaspheric plumes. *Journal of Geophysical Research: Space Physics*, *113*(A4). doi: 10.1029/2007JA012678

Summers, D., Omura, Y., Nakamura, S., & Kletzing, C. A. (2014). Fine structure of plasmaspheric hiss. *Journal of Geophysical Research: Space Physics*, *119*(11), 9134-9149. doi: 10.1002/2014JA020437

Takahashi, K., Mcentire, R. W., Lui, A. T. Y., & Potemra, T. A. (1990). Ion flux oscillations associated with a radially polarized transverse Pc 5 magnetic pulsation. *Journal of Geophysical Research: Space Physics*, *95*(A4), 3717-3731. doi: 10.1029/JA095iA04p03717

Thorne, R. M., Church, S. R., & Gorney, D. J. (1979). On the origin of plasmaspheric hiss: The importance of wave propagation and the plasmapause. *Journal of Geophysical Research: Space Physics*, *84*(A9), 5241-5247. doi: 10.1029/

JA084iA09p05241

Thorne, R. M., Li, W., Ni, B., Ma, Q., Bortnik, J., Baker, D. N., ... Angelopoulos, V. (2013). Evolution and slow decay of an unusual narrow ring of relativistic electrons near L 3.2 following the September 2012 magnetic storm. *Geophysical Research Letters*, *40*(14), 3507-3511. doi: 10.1002/grl.50627

Tsurutani, B. T., Falkowski, B. J., Pickett, J. S., Santolik, O., & Lakhina, G. S. (2015). Plasmaspheric hiss properties: Observations from Polar. *Journal of Geophysical Research: Space Physics*, *120*(1), 414-431. doi: 10.1002/2014JA020518

Tsurutani, B. T., Gonzalez, W. D., Gonzalez, A. L. C., Guarnieri, F. L., Gopalswamy, N., Grande, M., ... Vasyliunas, V. (2006). Corotating solar wind streams and recurrent geomagnetic activity: A review. *Journal of Geophysical Research: Space Physics*, *111*(A7). doi: 10.1029/2005JA011273

Wygant, J. R., Bonnell, J. W., Goetz, K., Ergun, R. E., Mozer, F. S., Bale, S. D., ... Tao, J. B. (2013). The Electric Field and Waves Instruments on the Radiation Belt Storm Probes Mission. *Space Science Review*, *179*, 183–220. doi: 10.1007/s11214-013-0013-7

Yang, B., Fu, S., Qiugang, Z., Yongfu, W., Xuzhi, Z., Zuyin, P., & Lun, X. (2008). Numerical study on ULF waves in a dipole field excited by sudden impulse. *Sci. China Ser. E-Technol. Sci.*, *151*, 1665-1676. doi: 10.1007/s11431-008-0251-1

Yang, B., Zong, Q.-G., Wang, Y. F., Fu, S. Y., Song, P., Fu, H. S., ... Reme, H. (2010). Cluster observations of simultaneous resonant interactions of ULF waves with energetic electrons and thermal ion species in the inner magnetosphere. *Journal of Geophysical Research: Space Physics*, *115*(A2). doi: 10.1029/2009JA014542

Yu, J., Li, L. Y., Cao, J. B., Chen, L., Wang, J., & Yang, J. (2017). Propagation characteristics of plasmaspheric hiss: Van Allen Probe observations and global empirical models. *Journal of Geophysical Research: Space Physics*, *122*(4), 4156-4167. doi: https://doi.org/10.1002/2016JA023372

Yue, C., Chen, L., Bortnik, J., Ma, Q., Thorne, R. M., Angelopoulos, V., ... Spence, H. E. (2017). The Characteristic Response of Whistler Mode Waves to Interplanetary Shocks. *Journal of Geophysical Research: Space Physics*, *122*(10), 10,047-10,057. doi: 10.1002/2017JA024574

Zhang, D., Liu, W., Li, X., Sarris, T. E., Wang, Y., Xiao, C., ... Wygant, J. R. (2020). Relation Between Shock-Related Impulse and Subsequent ULF Wave in the Earth's Magnetosphere. *Geophysical Research Letters*, *47*(23). doi: https://doi.org/10.1029/2020GL090027

Zhang, X. Y., Zong, Q.-G., Wang, Y. F., Zhang, H., Xie, L., Fu, S. Y., ... Pu, Z. Y. (2010). ULF waves excited by negative/positive solar wind dynamic pressure impulses at geosynchronous orbit. *Journal of Geophysical Research: Space Physics*, *115*(A10). doi: https://doi.org/10.1029/2009JA015016

Zhang, X. Y., Zong, Q. G., Yang, B., & Wang, Y. F. (2009). Numerical simulation of magnetospheric ULF waves excited by positive and negative impulses of solar wind dynamic pressure. *Sci. China Ser. E-Technol. Sci.*, *52*, 2886-2894. doi: 10.1007/s11431-009-0270-6

Zong, Q., Wang, Y., Yuan, C., Yang, B., Wang, C., & Zhang, X. (2011). Fast acceleration of "killer" electrons and energetic ions by interplanetary shock stimulated ULF waves in the inner magnetosphere. *China Science Bulletin*, *56*(1188). doi: 10.1007/s11434-010-4308-8

Zong, Q.-G., Zhou, X.-Z., Wang, Y. F., Li, X., Song, P., Baker, D. N., ... Pedersen, A. (2009). Energetic electron response to ULF waves induced by interplanetary shocks in the outer radiation belt. *Journal of Geophysical Research: Space Physics*, *114*(A10). doi: https://doi.org/10.1029/2009JA014393